Structural evidence for high-performance $PbZrO_3$-based antiferroelectrics by in-situ high-energy synchrotron X-ray diffraction

Hui Liu,[1,4] Longlong Fan,[1] Shengdong Sun,[1] Kun Lin,[1] Yang Ren,[3] Xiaoli Tan,[2] Xianran Xing,[1] and Jun Chen[1,]*

[1]Beijing Advanced Innovation Center for Materials Genome Engineering, and School of Mathematics and Physics, University of Science and Technology Beijing, Beijing 100083, China

[2]Department of Materials Science and Engineering, Iowa State University, Ames, Iowa 50011, USA

[3]X-Ray Science Division, Advanced Photon Source, Argonne National Laboratory, Argonne, Illinois 60439, USA

[4]Department of Physics, Central Michigan University, Mt. Pleasant, Michigan 48858, USA

*Corresponding author. junchen@ustb.edu.cn

Abstract

Antiferroelectrics (AFEs) have a great potential for modern electronic devices by virtue of the large electrostrain and unique polarization reversal during the antiferroelectric-to-ferroelectric (AFE-FE) phase transition under external electric fields. Although the fascinating macroscopic properties of AFE materials have been extensively studied, it is still unclear how the underlying structure evolution engenders their defining properties. Here we employ an electric biasing *in-situ* high-energy synchrotron X-ray diffraction technique to reveal the detailed structural evolution of a high performance $PbZrO_3$-based AFE material. During the reversible AFE-FE transition triggered by electric fields, the evolution of the superstructure is found to display strong dependence on the angle with respect to the field direction. Inactive domain switching and negligible lattice strain are observed in both the AFE and FE phases. Quantitative analysis of the *in-situ* diffraction data indicates that the high macroscopic electrostrain stems primarily from the crystal structure change during the abrupt AFE-FE phase transitions.

Keywords: Antiferroelectric ceramic; Electrostrain; Phase transition; In-situ X-ray diffraction.

1. Introduction

Antiferroelectrics (AFEs) have attracted increasing attention due to their potential for important applications such as energy storage and harvesting, actuators, electrocaloric cooling devices [1-9].The functionality of AFEs arises from a reversible transition between antiparallel and parallel dipole states under an externally applied electric field, so-called electric-field-induced AFE-to-FE transition, a process involving a large macroscopic electrostrain and polarization development [10-13]. The defining properties of these AEFs are strongly dependent on details of phase transition [5-7,14,15]. Therefore, understanding the transition in detail is a prerequisite for optimizing the design of high-performance AEFs, for instance achieving giant electrostrains at low electric field regime and reducing hysteresis of switching electric field.

The electric-field-induced AFE-to-FE transition has been extensively studied by macroscopic polarization, strain, and dielectric measurements [6,14,16,17]. Transmission electron microscopy (TEM) studies have also been conducted, and the recovery and destruction of AFE state have been observed [18-20]. X-ray and neutron diffraction studies have indicated changes in lattice strain and preferred orientation of domains during the AFE-to-FE transition [21-25]. In particular, Park *et al* have proposed a possible microstructural scenario of the AFE-to-FE switching sequence [21]. However, a complete picture between the structural evolution and their defining properties is still missing.

Interestingly, in situ high-energy synchrotron X-ray diffraction (SXRD) combined with 2D scattering technology has been demonstrated to be an exceptionally powerful tool for directly monitoring and quantifying the structural evolution of FEs/AFEs under an external electric field [26-31]. The technique benefits from the strong penetrating capability of high-energy synchrotron X-rays and the resulting ability to conduct experiments in transmission geometry, thereby avoiding the notorious surface layer effects [32], and thus enabling to reveal the intrinsic response of lattice to external electric fields. Owing to the high signal to noise ratio and high flux, the high-energy SXRD can probe the weak but very informative superstructure reflections which are typically related to AFEs. Note that the weak superstructure reflections are virtually impossible to observe with conventional XRD. Furthermore, the 2D geometry scattering technology simultaneously provides orientation-dependent information for anisotropic behaviors. Altogether, the technique enables the connection of the macroscopic properties with domain texture, lattice strain and crystal symmetry change during the electric field-induced AFE-to-FE transition.

Herein, we report the results of a comprehensive in-situ high-energy SXRD study on the evolution of the structure, domain texture, and lattice strain in one of the most representative perovskite AFEs – Nb doped $Pb(Zr,Sn,Ti)O_3$ ternary system, in particular $Pb_{0.99}\{Nb_{0.02}[(Zr_{0.57}Sn_{0.43})_{0.94}Ti_{0.06}]_{0.98}\}O_3$ (PNZST) composition [15]. We find strong evidences for the presence of strong correlation between superstructure evolution and polarization development in PNZST. Markedly, we are able to reproduce electrostrain in PNZST through a quantitative analysis of the high-energy SXRD. In particular, we show that the large electrostrain arises from an instantaneous large anisotropic lattice strain and a strong domain texture at the AFE to FE transition. The results will help the development of new AFE materials.

2. Experimental Section

The PNZST ceramic was fabricated by the solid-state reaction method. Analytic reagent grade PbO, Nb_2O_5, ZrO_2, SnO_2, and TiO_2 powders were used as raw materials. The homogeneous mixed powders were calcined at 850°C for 4 h and then sintered at 1300°C for 3 h. The details of the sample preparation can be seen in the ref. [16]. The relative density of the bulk ceramics is more than 95% of theoretical density and the average grain size is about 3μm. The *S*−*E* curves and *P*−*E* loops were measured on ceramic disks with a diameter of 8 mm, and thickness of 0.5 mm by using a standardized ferroelectric tester (aixACCT, TF Analyzer 1000).

For the in-situ high-energy SXRD measurements, the ceramic samples were polished, cut into rectangular bars with dimensions of 6 mm×1 mm×0.5 mm, and then annealed at 500 °C for 6 h to release stresses. Gold electrodes with a size of 6 mm×1 mm were evaporated on opposite faces of the bars. The in-situ high-energy SXRD measurements were conducted at the 11-ID-C beamline at the Advanced Photon Source (APS) at the Argonne National Laboratory. The X-ray beam with a spot size of 0.3 mm×0.3 mm, photon energy of about 110 keV and a wavelength of 0.11165 Å were used. A Perkin Elmer amorphous silicon 2D detector, positioned approximately 1800 mm away from the sample, was used to collect the scattered photons. The direction of the electric field was perpendicular to the X-ray beam. A triangular bipolar cycle electric field (−6 kV/mm ~ +6 kV/mm) with a step of about 0.5 kV/mm was applied to the bulk samples. At each step, a diffraction pattern was recorded with an acquisition time of 30 s, which is equivalent to a cyclic frequency around 40 mHz. The diffraction pattern of Ceria standard was used to calibrate the detector related parameters. The Debye rings collected on the 2D detector were divided into equidistant sectors at 15°. Intensities of the X-ray diffraction peaks in the sectors were integrated using the Fit2d software.

3. Results and discussion

3.1. Ferroelectric properties

Under applied electric field, the PNZST ceramic displays well-defined double hysteresis loops, which is a signature of AFEs (Fig. 1a). The measured critical field E_F (AFE to FE transition) and E_A (FE to AFE transition) is about 3.5 kV/mm, and 0.5 kV/mm, respectively. The maximum polarization of the FE phase is about 30 μC/cm^2. The macroscopic properties in the present study are consistent with the reported values in the literature [16]. To reveal the structural evolution of the PNZST ceramic induced by electric field, in situ high-energy SXRD was employed (Fig. 1b).

3.2. Evolution of the superstructure

A characteristic feature of AEFs is the intrinsic antiparallel atomic displacement, which manifests itself as a relatively weak but clearly discernible superstructure reflections in the respective diffraction patterns. Therefore, directly monitoring these superstructure reflections can help to understand the polarization development as revealed in the double *P-E* hysteresis loops. The evolution of the superstructure reflections parallel to the direction of the applied electric field ($\varphi = 0°$) is shown in Fig. 2. At the virgin AFE state, among the strong main Bragg reflections ($\boldsymbol{Q}_\mathrm{p}$), superstructure ½$(111)_\mathrm{p}$ and ½$(311)_\mathrm{p}$ reflections are observed at 1.5° and 2.6°, respectively. The reflections belong to $\boldsymbol{Q}_\mathrm{p}\pm$½$(111)_\mathrm{p}$-type superstructure reflections, and should be attributed to the octahedral tilting [33]. In addition, other superstructure reflections, marked with asterisks, are also seen. These indicate the presence of the incommensurate modulation and correspond to a modulation vector $\boldsymbol{q} = {}^1/_\mathrm{n}(110)_\mathrm{p}^*$ (*n* is about 7.8). Such incommensurate superstructure reflections can be attributed to the unique modulated atomic positions and responsible for the unique polarization of AFEs [13]. The incommensurate modulation vector in the present study is consistent with the pervious TEM study [18]. It has been suggested that such incommensurate structures result from the competing FE and AFE orderings [20,34]. With increasing electric field, no obvious change in the superstructure reflections is observed. When the field increases to 3.5 kV/mm near the shoulder of E_F, all superstructure reflections but the ½$(311)_\mathrm{p}$ reflection disappear. The observation indicates the emergence of AFE to FE transition. Note that the presence of the ½$(311)_\mathrm{p}$ superstructure reflection in the FE state is ascribed to the $a^-a^-a^-$ octahedral tilting, typical for rhombohedral *R*3*c* [33]. Upon unloading the electric field below 0.5 kV/mm which is near the measured E_A, the superstructure reflections reappear. These features repeat in the subsequent cycle of electric field, indicating a reversible electric field induced AFE-to-FE transition. Notably, such an evolution of incommensurate reflections has also been observed with in-situ TEM and neutron diffraction studies [18,23]. When the intensity of these superstructure reflections is compared with the double *P*-*E* hysteresis loops (Fig. 3), one can notice the existence of a strong correlation. It suggests that the electric-field-induced polarization is highly correlated with the intrinsic atomic ordering.

It is interesting to observe that the intensity of superstructure reflections for both AFE and FE exhibits strong anisotropy after exposure to electric fields (Fig. 4). Significant differences are observed in the $\frac{1}{2}(111)_p$ superstructure reflection between the virgin and the field exposed AFE state. The intensity of $\frac{1}{2}(111)_p$ reflections at the virgin state is the same over all orientations, whereas in the field exposed sample it appears enhanced along the electric field direction ($\varphi = 0°$), and suppressed in the perpendicular direction ($\varphi = 90°$) (Fig. 4a). It implies that the initially random AFE domains develop a texture after the FE-AFE transition takes place. On the contrary, the $\frac{1}{2}(311)_p$ reflections of the FE state show high intensity at $\varphi = 90°$ and low intensity at $\varphi = 0°$ (Fig. 4b). This scenario has also been observed in the electric-field-induced rhombohedral (*R*3*c*) phase in $(Bi_{1/2}Na_{1/2})TiO_3$-based Pb-free FEs [35,36]. It can be ascribed to strain-induced anisotropic octahedral tilting, but not to domain texturing because no splitting of this reflection is noticed.

3.3. Domain texture and lattice strain analysis

Figures 5(a-c) show the $\{110\}_p$, $\{111\}_p$ and $\{200\}_p$ profiles, respectively, under a full cycle of bipolar electric fields at $\varphi = 0°$, 45° and 90°. At the virgin state, it is evident that the $\{200\}_p$ and $\{111\}_p$ profiles split into two reflections, suggesting an orthorhombic symmetry. For the AFE_O, the $(110)_p$

should split, but the diffraction resolution in the present study is insufficient to reveal. With increasing electric field, all the reflections remain largely unchanged until 3.5 kV/mm, which corresponds to the measured E_F. At this critical electric field, the split $\{200\}_\mathrm{p}$ reflections merge into a singlet, suggesting the AFE$_O$ to FE$_R$ transition. The instantaneous peak position shift of $\{110\}_\mathrm{p}$ is accompanied by intensity interchange of the $\{111\}_\mathrm{p}$ reflection, which suggests an orientation dependent lattice strain and domain texture development. With further increasing electric field, FE$_R$ is stable with no obvious changes in its superstructures. Upon decreasing the electric field to 0.5 kV/mm, the singlet $\{200\}_\mathrm{p}$ reflection splits into doublet, and the $\{110\}_\mathrm{p}$ and $\{111\}_\mathrm{p}$ reflections shift back to the high angle side, indicating that the FE$_R$ switches back to AFE$_O$. In contrast to the virgin AFE$_O$, the $\{200\}_\mathrm{p}$ reflection for the poled sample exhibits a strong texture. Under the subsequent cycle of applied electric field, this scenario repeats itself. It is noted that the $\{200\}_\mathrm{p}$ reflection changes negligibly in both intensity and position. This suggests that the external electric field can hardly develop any texture in AFE. Such a reversible AFE$_O$ to FE$_R$ transition is in line with the observed evolution in the superstructure reflections (Fig. 2). In addition, similar evolution of the {210} profile is also evident (Fig. 6).

It is well known that the polarization of FE$_R$ occurs along the $[111]_\mathrm{p}$ direction. Thus the domain texture can be evaluated from the change of intensity of the $\{111\}_\mathrm{p}$ profile. For AFE$_O$ with incommensurate modulations, the polarization is considered to lie within the $(110)_\mathrm{p}$ plane, but the detailed polarization configuration remains unknown. Here, the interchange of intensity of the $\{200\}_\mathrm{p}$ profile was used to estimate the domain texture of AFE$_O$. In order to quantify the electric-field-induced domain texture and lattice strain, the $\{111\}_\mathrm{p}$ reflections for FE$_R$ and AFE$_O$ and the $\{200\}_\mathrm{p}$ reflections for AFE$_O$ were fitted with doublets with a pseudo-Voigt shape, while a single one was used to fit the $\{200\}_\mathrm{p}$ profile of FE$_R$ and $(110)_\mathrm{p}$ profiles.

The domain texture can be described by the multiple random distribution (*f*) function. The f_{200} of AFE$_O$ and f_{111} of FE$_R$ can be calculated by the following equations (1) and (2), respectively: [37]

$$f_{200} = 3 \times \frac{I_{200}^{E}/I_{200}^{0}}{I_{200}^{E}/I_{200}^{0}+2I_{002}^{E}/I_{002}^{0}} \qquad (1)$$

$$f_{111} = 4 \times \frac{I_{111}^{E}/I_{111}^{0}}{I_{111}^{E}/I_{111}^{0}+3I_{11\bar{1}}^{E}/I_{11\bar{1}}^{0}} \qquad (2)$$

where I_{hkl}^{E} is the integrated intensity of *hkl* reflection under electric field, I_{hkl}^{0} is the integrated intensity of *hkl* reflection at the virgin state. For the FE$_R$, the ideal $I_{111}^{0}/I_{11\bar{1}}^{0}$ = 1/3 is used for the calculation. The values of f_{200} and f_{111} are identical to be 1 at the unpoled state, while 3 and 4 at the saturated state, respectively. According to the Bragg law, $2d_{hkl}\sin\theta = n\lambda$, the value of d_{hkl} can be obtained. The lattice strain can be calculated by:

$$\varepsilon = \frac{d_E - d_0}{d_0} \qquad (3)$$

where d_E is the lattice spacing under electric field *E*, d_0 is lattice spacing at virgin state.

The value of f_{200} of AFE$_O$ is shown in Fig. 7a as a function of the orientation at representative electric fields. The value f_{200} of AFE$_O$ stays constant in the sub-critical field regime. It indicates that non-180° domain reorientation does not occur when an electric field is applied. It is analogous to the observation that non-180° domain alignment takes place at the sub-coercive fields for unpoled piezoceramics. However, the domain texture emerges in AFE$_O$ during and after the electric field unloading; such a texture preserves in the subsequent electric field cycles. This indicates that the domain texture in AFE$_O$ is inherited from FE after the FE-to-AFE transition in the first cycle of electric field. Non-180° domain switching is not observed to occur in the subsequent cycles of electric field. In contrast, the FE$_R$ immediately exhibits a high domain texture once it is induced by applied field (Fig. 7b). For instance, the value of f_{111} is 3.12 at E = 6 kV/mm along the electric field direction ($\varphi = 0°$). It reaches a value 87% of the saturated state. The value is comparable to the FE$_R$ of $PbZr_{0.55}Ti_{0.45}O_3$

(PZT55, 3.48) and $0.6PbTiO_3$-$0.4BiScO_3$ (PT-40BS, 2.5) [38,39]. It changes little under further applied electric fields once it is induced. In other words, non-180° domain reorientation hardly occurs under electric fields in both the AFE and the FE states. Consequently, the large electrostrain must be attributed to the intrinsic lattice strain at the phase transition.

Figure 8 shows the calculated lattice strains of the characteristic $\{110\}_p$ profile, $(111)_p$ and $(200)_p$ reflection as a function of the bipolar electric field. Interestingly, these calculated lattice strains exhibit a shape similar to that of the measured *S-E* curves. Negligible lattice strain is observed for the virgin AFE state, while a small amount of residual strain is observed in the poled AFE. There is an abrupt change near the critical electric field which marks the AFE-to-FE transition. The change is accompanied with the emergence of orientation dependent behaviors observed in piezoelectric materials. Specifically, at E = 6 kV/mm, $\varepsilon_{(200)_p}$ is 0.06% at 0°, while it is negative, –0.02% and –0.16%, respectively, for 45° and 90° (Fig. 8a). As a comparison, the observed $\varepsilon_{(200)_p}$ at $\varphi = 0°$ is much lower than the FE_R of PZT55 (0.20%) [38]. The corresponding piezoelectric response of the metastable FE_R is about 110 pm/V, which is much lower than that of rhombohedral PZT55 (330 pm/V) and PT-40BS (440 pm/V) [38,39]. It demonstrates that the induced FE_R phase is frustrated by the phase transition. It is worth mentioning that the value of $\varepsilon_{(200)_p}$ is slightly positive at 0° but strongly negative at 90° after the AFE-to-FE transition. It is due to the change of polarization direction during the transition. On the contrary, the values of $\varepsilon_{\{110\}p}$ and $\varepsilon_{(111)p}$ are positive for all orientations. In particular, large values are observed along the applied electric field and relatively low values are observed in directions off the electric field. The present results lead to the conclusion that the AFE materials exhibit negligible domain switching but large lattice strain through the AFE_O to FE_R transition.

3.4. Estimation of macroscopic strains

It is acknowledged that the macroscopic electrostrain of piezoelectric materials originates from intrinsic structural contributions, including lattice strain, structural transformation, and extrinsic contributions of domain wall motion. In the present study, since negligible domain switching is observed in both AFE$_O$ and FE$_R$ (Fig. 7), it indicates that the macroscopic electrostrain originates from intrinsic structural contributions but not the extrinsic contributions. The intrinsic strain contribution can be estimated by the approach described in ref. [40] as given by equation (4):

$$S_\varphi = \frac{\sum_{hkl} f_{hkl}(\varphi) m_{hkl} \varepsilon_{hkl}(\varphi)}{\sum_{hkl} f_{hkl}(\varphi) m_{hkl}(\varphi)} \tag{4}$$

where $f_{hkl}(\varphi)$ denotes the domain texture with orientation φ to the electric field, and m_{hkl} denotes the multiplicity of *hkl* reflections. For *hkl* reflections that do not have domain texture, the f_{hkl} value is 1. In this study, the characteristic $\{200\}_p$, $\{110\}_p$ and $\{111\}_p$ profiles are used for the estimation. This strategy was used in the previous studies on piezoceramics [41,42]. The calculated strain corresponds to the longitudinal strain (S_{33}) at $\varphi = 0°$, and to the transverse strain (S_{11}) at $\varphi = 90°$. The volume strain (S_V) is calculated as $S_{33}+2S_{11}$.

Figure 9 presents a comparison between the calculated and measured strains as a function of the applied bipolar electric field. Intriguingly, there are very good agreements between the calculated lattice strains and the measured ones for the longitudinal, transverse, and volume strains. The calculated strain abruptly increases at E_F = 3.5 kV/mm during loading of electric field, and abruptly drops at E = 0.5 kV/mm during unloading. These critical fields correspond to the E_F and E_A measured by the macroscopic *S*-*E* curves, respectively. The calculated S_{33} and S_{11} at E = 6 kV/mm is 0.30%, and 0.073%, respectively. Both approximate the measured ones (x_{33} = 0.28, x_{11} = 0.070%). It needs to note that the measured negative transverse x_{11} (about −0.02%) during the second cycle of applied electric fields can be also reproduced by the quantification (S_{11} = –0.021%). The calculated piezoelectric response (d_{33}^*) of the induced FE state is 76 pm/V, which is very close to the measured one (74 pm/V). In addition, the calculated volume strain S_V at E = 6 kV/mm is 0.45%, which is slightly higher than the measured one (0.42%). Compared with piezoelectric materials, the large electrostrain in AFE stems from structural phase transition, which generates large lattice strain and restructures the local atomic ordering.

Based on the results revealed in this in situ study, a revised AFE-FE switching sequence is presented in Fig. 10. The randomly oriented AFEs at virgin state remains under applied electric field. This scenario is consistent with a recent observation [25], but is different from the pervious assumption made by Park *et al* [21], in which the randomly oriented AFE$_O$ is forced to orient preferentially. When the electric field reaches E_F, the randomly oriented AFE$_O$ switches into highly domain textured FE$_R$. After that, the sample cannot resume its virgin state. Under applied electric field beyond E_F, there is very limited domain reorientation and lattice strain in the induced FE$_R$. Strong domain texture is developed once the FE$_R$ is formed at the phase transition. When the electric field is removed, the FE$_R$ transforms into AFE$_O$ with a texture.

4. Conclusions

In summary, the detailed picture of the structural evolution correlating with electrostrain and polarization development is elucidated for a typical $PbZrO_3$-based AFE ceramic using advanced in-situ high-energy SXRD. Structural data provide strong evidences for the presence of the electric-field-induced reversible AFE-FE transition and superstructure evolution, both of which are highly correlated. Both the AFE and the FE phase exhibit negligible domain reorientation and lattice strain under applied electric field, and the induced FE phase display moderate piezoelectricity. The excellent agreement between measured and computed electrostrains demonstrates that the large macroscopic electrostrain stems from intrinsic structural contributions of the crystal structure change and the strong texture in the induced FE phase at the phase transition. These results provide a clear microstructural description of the material response to applied electric fields, and are helpful for the development of new AFE materials for applications in actuators and electrocaloric cooling devices.

Acknowledgements

This work was supported by the National Natural Science Foundation of China (Grant Nos. 21825102, 21731001, and 21590793), and the Fundamental Research Funds for the Central Universities, China (Grant No. FRF-TP-17-001B). H. L. thanks the financial support from China Scholarship Council and X.T. acknowledges the financial support by the U.S. National Science Foundation (NSF) through Grant DMR-1700014. This research used resources of the Advanced Photon Source, a U.S. Department of Energy (DOE) Office of Science User Facility operated for the DOE Office of Science by Argonne National Laboratory under Contract No. DE-AC02-06CH11357.

References

[1] A.S. Mischenko, Q. Zhang, J.F. Scott, R.W. Whatmore, N.D. Mathur, Giant electrocaloric effect in thin-film $PbZr_{0.95}Ti_{0.05}O_3$, Science 311 (2006) 1270-1271.

[2] B. Xu, J. Íñiguez, L. Bellaiche, Designing lead-free antiferroelectrics for energy storage, Nat. Commun. 8 (2017), 15682.

[3] J. Li, F. Li, Z. Xu, S. Zhang, Multilayer lead-free ceramic capacitors with ultrahigh energy density and efficiency, Adv. Mater. 30 (2018), 1802155.

[4] L. Yang, X. Kong, F. Li, H. Hao, Z. Cheng, H. Liu, J. Li, S. Zhang, Perovskite lead-free dielectrics for energy storage applications, Prog. Mater. Sci. 102 (2019) 72-108.

[5] L. Zhao, Q. Liu, J. Gao, S. Zhang, J. Li, Lead-free antiferroelectric silver niobate tantalate with

high energy storage performance, Adv. Mater. 29 (2017), 1701824.

[6] F. Zhuo, Q. Li, Y. Zhou, Y. Ji, Q. Yan, Y. Zhang, W. Cao, Large field-induced strain, giant strain memory effect, and high thermal stability energy storage in (Pb,La)(Zr,Sn,Ti)O_3 antiferroelectric single crystal, Acta Mater. 148 (2018) 28-37.

[7] A. Pérez-Tomás, M. Lira-Cantú, G. Catalan, Above-bandgap photovoltages in antiferroelectrics, Adv. Mater. 28 (2016) 9644-9647.

[8] S. Zhang, A.B. Kounga, W. Jo, C. Jamin, K. Seifert, T. Granzow, J. Rödel, D. Damjanovic, High-strain lead free antiferroelectric electrostrictors, Adv. Mater 21 (2009) 4716-4720.

[9] R.Z. Zuo, J. Fu, H. Qi, Stable antiferroelectricity with incompletely reversible phase transition and low volume-strain contribution in $BaZrO_3$ and $CaZrO_3$ substituted $NaNbO_3$ ceramics, Acta Mater. 161 (2018) 352-359.

[10] C. Kittel, Theory of antiferroelectric crystals, Phys. Rev. 82 (1951) 729-732.

[11] E. Sawaguchi, H. Maniwa, S. Hoshino, Antiferroelectric structure of lead zirconate, Phys. Rev. (83) 1951, 1078.

[12] A.K. Tagantsev, K. Vaideeswaran, S.B. Vakhrushev, A.V. Filimonov, R.G.Burkovsky, A. Shaganov, D. Andronikova, A.I. Rudskoy, A.Q.R. Baron, H.Uchiyama, D. Chernyshov, A. Bosak, Z. Ujma, K. Roleder, A. Majchrowski, J.H. Ko, N. Setter, The origin of antiferroelectricity in $PbZrO_3$, Nat. Commun. 4 (2013), 2229.

[13] I. MacLaren, R. Villaurrutia, B. Schaffer, L. Houben, A. Pelaiz-Barranco, Atomic-scale imaging and quantification of electrical polarisation in incommensurate antiferroelectric lanthanum-doped lead zirconate titanate, Adv. Funct. Mater. 22 (2012) 261-266.

[14] X. Hao, J.W. Zhai, L.B. Kong, Z.K. Xu, A comprehensive review on the progress of lead zirconate-based antiferroelectric materials, Prog. Mater. Sci. 63 (2014) 1-57.

[15] X. Tan, C. Ma, J. Frederick, S. Beckman, K.G. Webber, The antiferroelectric↔ferroelectric phase transition in lead-containing and lead-free perovskite ceramics, J. Am. Ceram. Soc. 94 (2011) 4091-

4107.

[16] J. Frederick, X. Tan, W. Jo, Strains and polarization during antiferroelectric-ferroelectric phase switching in $Pb_{0.99}Nb_{0.02}((Zr_{0.57}Sn_{0.43})_{1-y}Ti_y)_{0.98}O_3$ ceramics, J. Am. Ceram. Soc. 94 (2011) 1149-1155.

[17] F. Zhuo, Q. Li, J.H. Gao, Q. Yan, Y. Zhang, X. Xi, X. Chu, Phase transformations, anisotropic pyroelectric energy harvesting and electrocaloric properties of $(Pb,La)(Zr,Sn,Ti)O_3$ single crystals, Phys. Chem. Chem. Phys. 19 (2017) 13534-13546.

[18] H. He, X. Tan, Electric-field-induced transformation of incommensurate modulations in antiferroelectric $Pb_{0.99}Nb_{0.02}((Zr_{1-x}Sn_x)_{1-y}Ti_y)_{0.98}O_3$, Phys. Rev. B 72 (2005), 024102.

[19] H. Guo, X. Tan, Direct observation of the recovery of an antiferroelectric phase during polarization reversal of an induced ferroelectric phase, Phys. Rev. B 91 (2015), 144104.

[20] Z. Xu, X. Dai, Viehland, D. Impurity-induced incommensuration in antiferroelectric La-modified lead zirconate titanate, Phys. Rev. B 51 (1995), 6261.

[21] S.E. Park, M.J. Pan, K. Markowski, S. Yoshikaw, and L.E. Cross, Electric field induced phase transition of antiferroelectric lead lanthanum zirconate titanate stannate ceramics, J. Appl. Phys. 82 (1997) 1798-1803.

[22] X. Tan, J. Frederick, C. Ma, W. Jo, J. Rödel, Can an electric field induce an antiferroelectric phase out of a ferroelectric phase? Phys. Rev. Lett. 105 (2010), 255702.

[23] T. Lu, A.J. Studer, D. Yu, R.L. Withers, Y. Feng, H. Chen, S.S. Islam, Z. Xu, Y. Liu, Critical role of the coupling between the octahedral rotation and A-site ionic displacements in $PbZrO_3$-based antiferroelectric materials investigated by in situ neutron diffraction, Phys. Rev. B (96) 2017, 214108.

[24] I.V. Ciuchi, C.C. Chung, C.M. Fancher, J. Guerrier, J.S. Forrester, J.L Jones, C. Galassi, Field-induced antiferroelectric to ferroelectric transitions in $(Pb_{1-x}La_x)(Zr_{0.90}Ti_{0.10})_{1-x}O_3$ investigated by in situ X-ray diffraction, J. Eur. Ceram. Soc. (37) 2017 4631-4636.

[25] T. Lu, A.J. Studer, L. Noren, W. Hu, D. Yu, B. McBride, Y. Feng, R.L. Withers, H. Chen, Z.

Xu, Y. Liu, Electric-field-induced AFE-FE transitions and associated strain/preferred orientation in antiferroelectric PLZST, Sci. Rep. 6 (2015), 23659.

[26] H. Liu, J. Chen, L. Fan, Y. Ren, Z. Pan, K.V. Lalitha, J. Rödel, X. Xing, Critical role of monoclinic polarization rotation in high-performance perovskite piezoelectric materials, Phys. Rev. Lett. 119 (2017), 017601.

[27] H. Liu, J. Chen, H. Huang, L. Fan, Y. Ren, Z. Pan, J. Deng, L.Q. Chen, X. Xing, Role of reversible phase transformation for strong piezoelectric performance at the morhpotropic phase boundary, Phys. Rev. Lett. 120 (2018), 055501.

[28] Y. Li, Y. Chen, Z. Zhang, A. Kleppe, D.A. Hall, In-situ XRD study of actuation mechanisms in $BiFeO_3$-$K_{0.5}Bi_{0.5}TiO_3$-$PbTiO_3$ ceramics, Acta Mater. 168 (2019) 411-425.

[29] A. Pramanick, D. Damjanovic, J.E. Daniels, J.C. Nino, J.L. Jones, Origins of electro-mechanical coupling in polycrystalline ferroelectrics during subcoercive electrical loading, J. Am. Ceram. Soc. 94 (2011) 293-309.

[30] M. Hinterstein, M. Hoelzel, J. Rouquette, J. Haines, J. Glaum, H. Kungl, M. Hoffman, Interplay of strain mechanisms in morphotropic piezoceramics, Acta Mater. 94 (2015) 319-327.

[31] J. Schultheiß, L. Liu, H. Kungl, M. Weber, L.K. Venkataraman, S. Checchia, D. Damjanovic, J.E. Daniels, J. Koruza, Revealing the sequence of switching mechanisms in polycrystalline ferroelectric/ferroelastic materials, Acta Mater. 157 (2018) 355-363.

[32] T. Lu, A.J. Studer, D. Cortie, K. Lau, D. Yu, Y. Feng, H. Chen, Z. Xu, R.L. Withers, G.J. McIntyre, Y. Liu, Susceptible ferroelectric/antiferroelectric phase transition near the surface of Nb-doped lead zirconate stannate titanate from surface processing. ACS Appl. Mater. Interf. (8) 2016 14313-14317.

[33] M. Glazer, The classification of tilted octahedra in perovskites. Acta Crystallogr, Sect. B (28) 1972, 3384.

[34] E.V. Balashova, A.K. Tagantsev, Polarization response of crystals with structural and ferroelectric instabilities, Phys. Rev. B 48 (1993), 9979.

[35] H. Simons, J. Daniels, W. Jo, R. Dittmer, A. Studer, M. Avdeev, J. Rödel, M. Hoffman, Electric-field-induced strain mechanisms in lead-free 94%$(Bi_{1/2}Na_{1/2})TiO_3$-6%$BaTiO_3$, Appl. Phys. Lett. (98) 2011, 082901.

[36] M. Acosta, L.A. Schmitt, C. Cazorla, A. Studer, A. Zintler, J. Glaum, H.J. Kleebe, W. Donner, M. Hoffman, J. Rödel, M. Hinterstein, Piezoelectricity and rotostriction through polar and non-polar coupled instabilities in bismuth-based piezoceramics, Sci. Rep. 6 (2016) 28742.

[37] J.L. Jones, E.B. Slamovich, K.J. Bowman, Domain texture distributions in tetragonal lead zirconate titanate by x-ray and neutron diffraction, J. Appl. Phys. 97 (2005), 034113.

[38] L. Fan, J. Chen, Y. Ren, X. Xing, Structural correlation to piezoelectric and ferroelectric mechanisms in rhombohedral $Pb(Zr,Ti)O_3$ ceramics by in-situ synchrotron diffraction, Inorg. Chem. (57) 2018 3002-3007.

[39] K.V. Lalitha, C.M. Fancher, J.L. Jones, R. Ranjan, Field induced domain switching as the origin of anomalous lattice strain along non-polar direction in rhombohedral $BiScO_3$-$PbTiO_3$ close to the morphotropic phase boundary, Appl. Phys. Lett. 107 (2015), 052901.

[40] M.R. Daymond, The determination of a continuum mechanics equivalent elastic strain from the analysis of multiple diffraction peaks, J. Appl. Phys. 96 (2004) 4263-4272.

[41] C. Zhao, D. Hou, C.-C. Chung, H. Zhou, A. Kynast, E. Hennig, W. Liu, S. Li, J.L. Jones, Deconvolved intrinsic and extrinsic contributions to electrostrain in high performance Nb-doped Pb $(Zr_xTi_{1-x})O_3$ piezoceramics ($0.50 \leq x \leq 0.56$), Acta Mater. 158 (2018) 369-380.

[42] M.C. Ehmke, N.H. Khansur, J.E. Daniels, J.E. Blendell, K.J. Bowman, Resolving structural contributions to the electric-field-induced strain in lead-free $(1-x)Ba(Zr_{0.2}Ti_{0.8})O_3-x(Ba_{0.7}Ca_{0.3})TiO_3$ piezoceramics, Acta Mater. 66 (2014) 340-348.

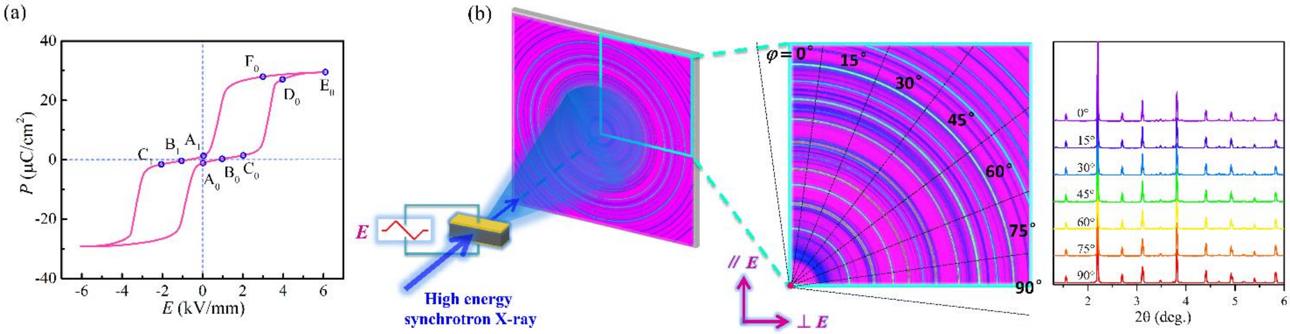

Figure 1. (a) P-E hysteresis loops of PNZST ceramics measured at room temperature at 1 Hz. The letters indicate different polarization states. (b) Schematic of the experimental setup for in-situ high-energy synchrotron X-ray diffraction experiments.

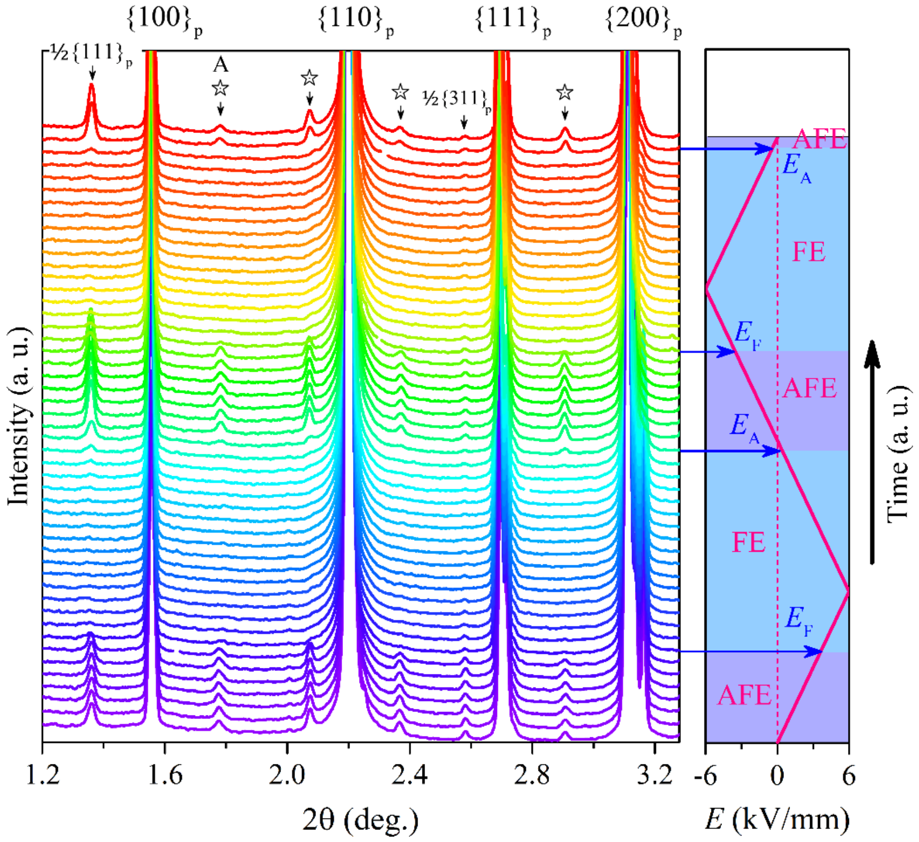

Figure 2. Evolution of satellite peaks as function of bipolar electric field at $\varphi = 0°$. The incommensurate peaks are marked with asterisks.

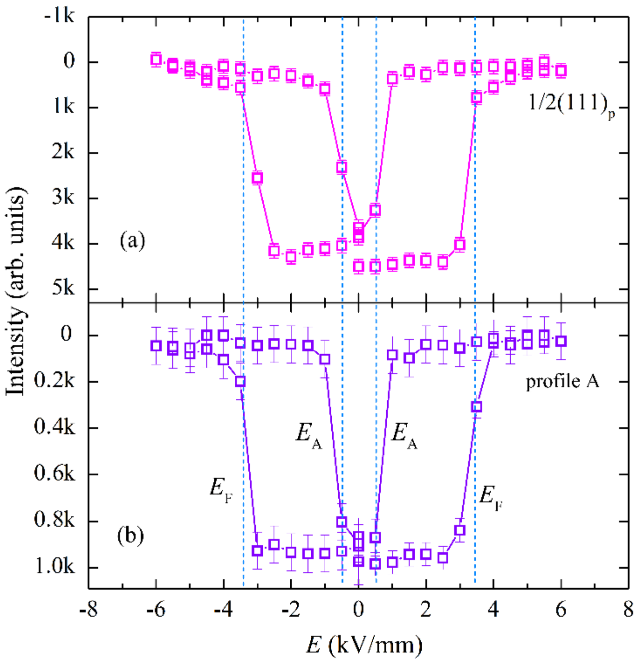

Figure 3. The integrated intensity of commensurate ½(111)$_p$ (a), and incommensurate profile A (b) with the applied bipolar electric field.

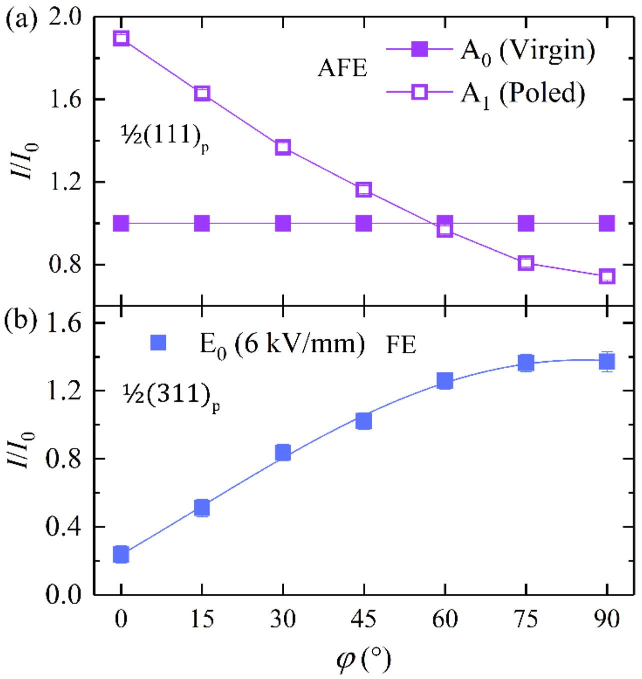

Figure 4. (a) Ratio of the integrated intensity of the superstructure ½(111)$_p$ reflection of AEF phase, and (b) the ½(311)$_p$ reflection of EF phase as a functions of φ at various electric field.

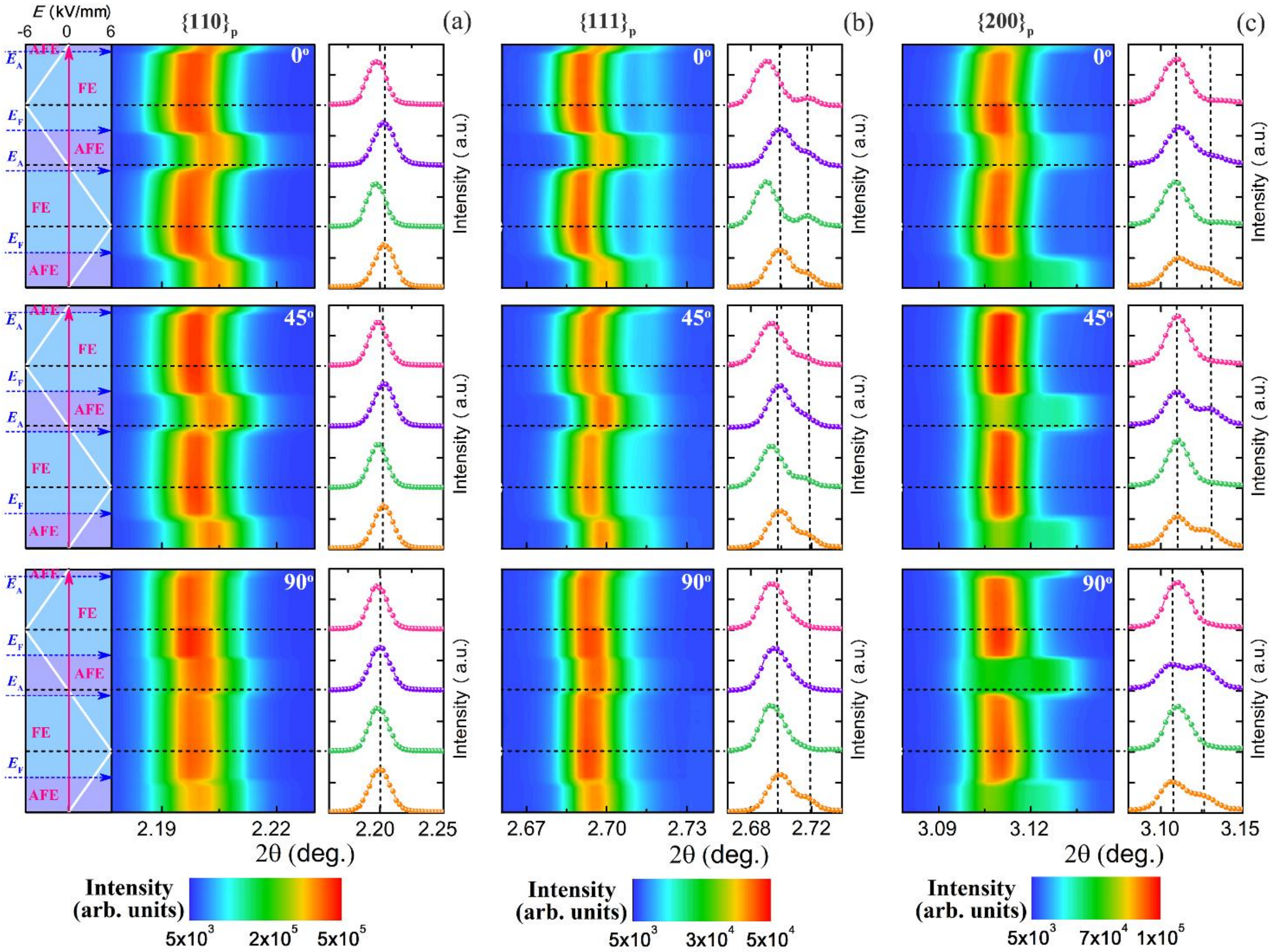

Figure 5. Contour plots of in situ diffraction patterns. (a) Evolution of $(110)_p$, (b) $(111)_p$, and (c) $(200)_p$ profiles as a function of bipolar electric field at $\varphi = 0°$, 45° and 90°. The patterns on right-hand of each contour plot correspond to the profile at the virgin AFE state (yellow), positive maximum electric field of the FE state (green), zero field of the poled AFE state (purple), and at negative maximum electric field of the FE state (pink). The dashed line represents the profile center for the virgin state.

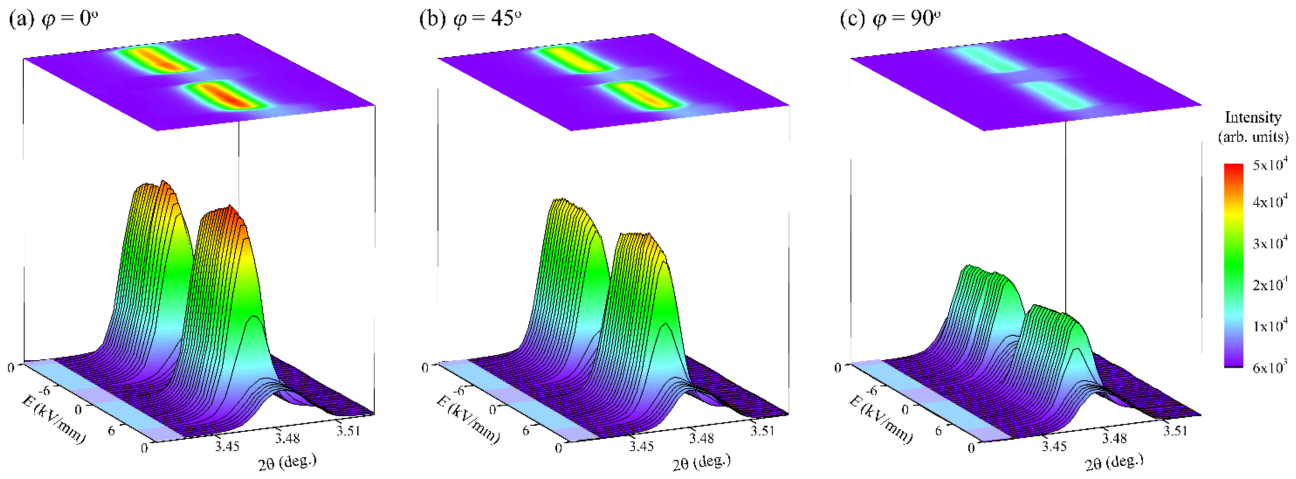

Figure 6. Contour plots of $\{210\}_{\text{p}}$ profile during applied electric field. (a) $\varphi = 0°$, (b) $\varphi = 45°$ and (c) $\varphi = 90°$.

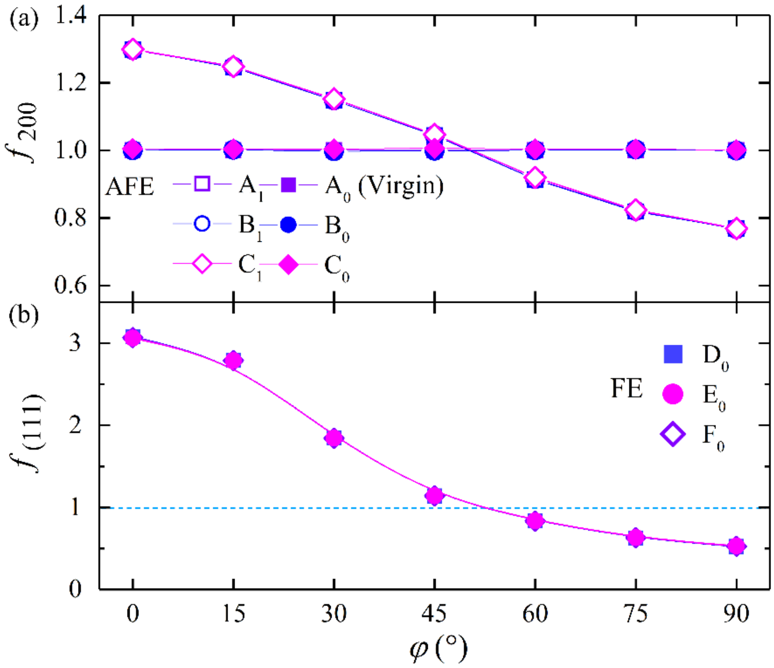

Figure 7. (a) f_{200} for the antiferroelectric phase, and (b) $f_{(111)}$ for the ferroelectric phase as a function of orientation (φ) and various electric fields. The states of electric field, indicated by letters, can be referred to Fig. 1a.

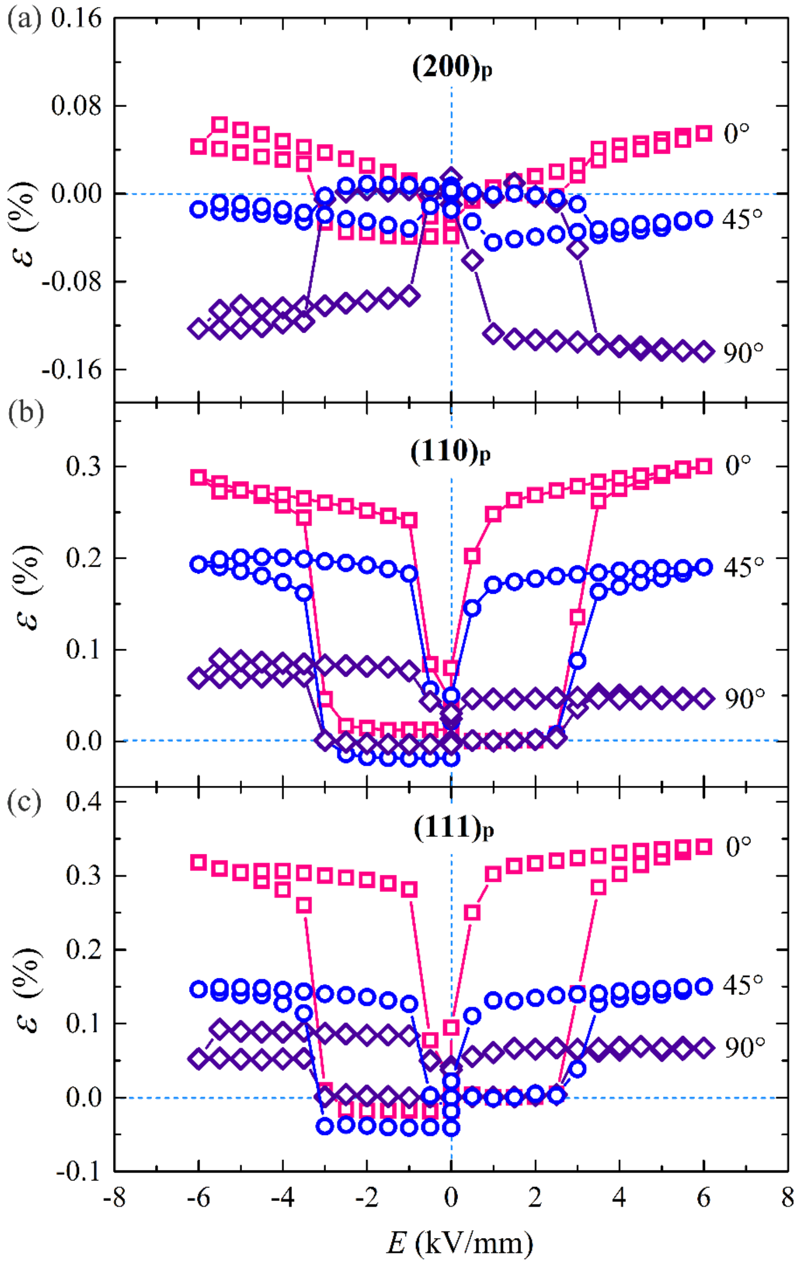

Figure 8. (a) Calculated lattice strain of (a) $(200)_p$, (b) $(110)_p$, and (c) $(111)_p$ reflections as a function of bipolar electric field.

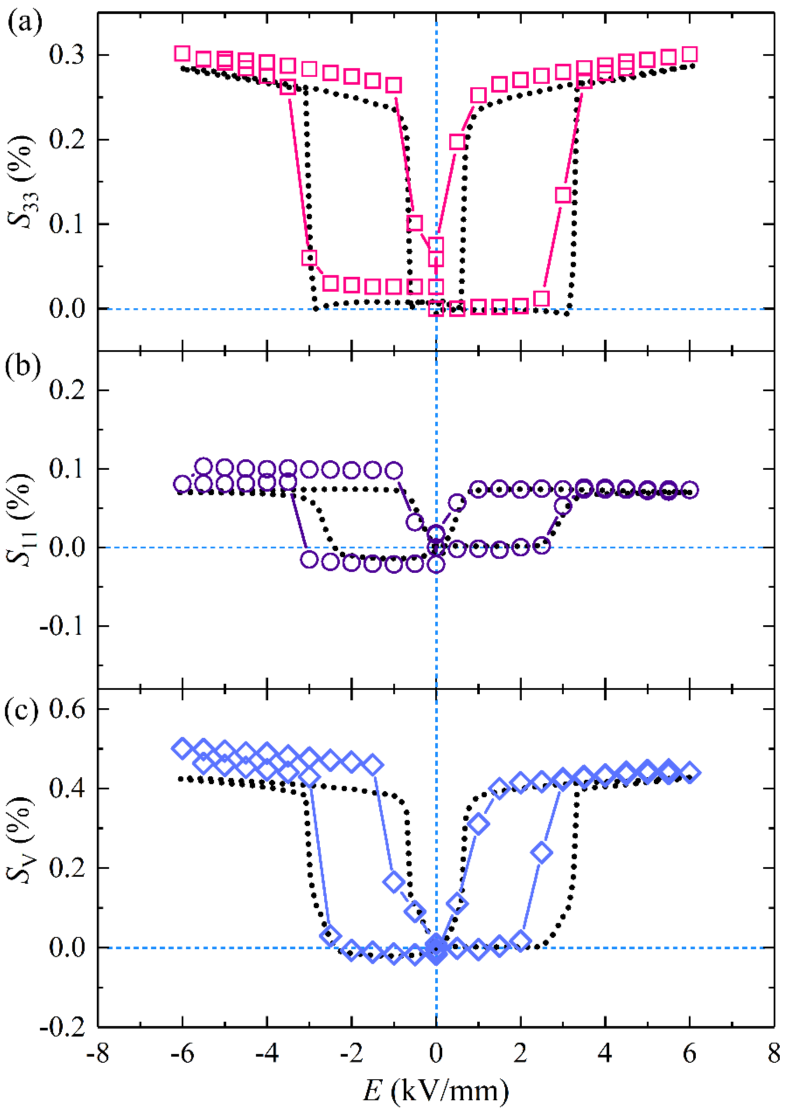

Figure 9. Comparison between the calculated (hollow point) and the macroscopic measured strain (black point) in the PNZST ceramics as a function of applied electric field: (a) longitudinal strain, (b) transverse strain, and (c) volume strain. The macroscopic measured strain is taken from Ref. [16].

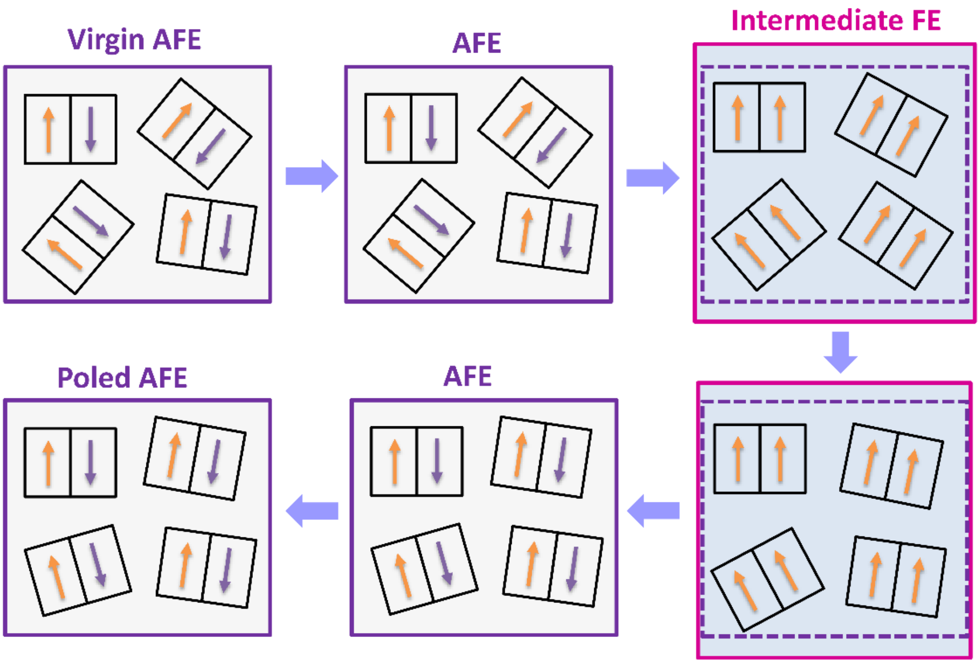

Figure 10. Simplified schematic diagram of AFE-to-FE switching sequence.

I think the two intermediate AFE states are more like the following. If you guys agree, you may make changes to other panels accordingly. Also we need to make it clear that such a difference occurs only in the very first exposure to electric field. There is no further changes in successive cycles.

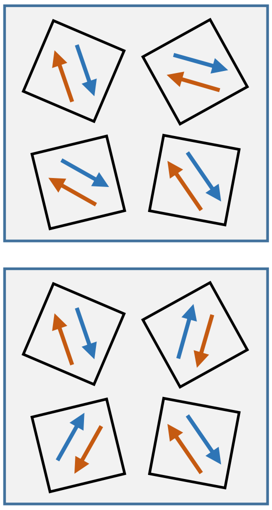

Graphical Abstract